Twofold ion effect to develop PANI@$MgCoO_2$ nanocomposites for magnesium batteries

Kahla Missaoui
Tunis El Manar University
Karima Ferchichi
Tunis El Manar University
Noureddine Amdouni
Tunis El Manar University
Daniel Cosano
University of Córdoba
Rui Liu
Shandong University of Science and Technology
Siyuan Pan
Xiamen University
He Zhanning
Xiamen University
Yong Yang
Xiamen University
Gregorio F. Ortiz (g_ortiz@163.com)
Xiamen University

Research Article

Keywords: MgCoO2, Conducting Polymer, Pickering emulsion composite materials, hybrid battery

Posted Date: March 24th, 2023

DOI: https://doi.org/10.21203/rs.3.rs-2686581/v1

Abstract

A cost-effective method for obtaining polyaniline coated magnesium cobalt oxide nanocomposites (PANI@$MgCoO_2$) as potential cathode material for rechargeable magnesium batteries (RMB) is reported. Structural characterizations confirm the presence of a thin layer of conducting polymer on the particles of the cubic oxide that enhanced the cycling life of the battery as compared to the pristine material. To develop the electrochemical performance a twofold combination of sodium and magnesium ion is employed. The 15%PANI@$MgCoO_2$ nanocomposites exhibited enhanced reversible capacity (103.4 – 153 mA h g^{-1}) at ~ 1 V vs. Mg^{2+}/Mg as compared to pristine material. X-ray diffraction patterns revealed a single-phase insertion/extraction reaction mechanism into/from the cubic structure. These results establish a useful methodology for employing PANI coating on other oxides with applicability in batteries.

1. Introduction

Rechargeable magnesium batteries (RMB) are considered as a promising battery technology to complement the future generation of energy storage devices[1]. RMBs are a good contender due to their high safety and low cost as compared to the well-known Li-ion technology [2]. Within the useful family of structures, magnesium-based oxides are highly competitive as electrode materials of RMBs,[3–6] which in future may find application for large-scale application, standing at the vanguard of the energy storage[7, 8].

On the lithium part, the $LiCoO_2$ cathode reacts through intercalation/de-intercalation of mobile Lithium (Li^+) ions into the layered crystal structure which can reach a theoretical capacity of 273 mA h g^{-1} per intercalated ion (in fact only around 0.5 lithium atoms/fu can be reversibly intercalated) [9]. To construct a Li-ion battery the $LiCoO_2$ is combined with a lithium-free host material like graphite anode because lithium metal anode is hazardous. Unless a solid electrolyte is employed in the cell combined with a proper lithium metal oxide cathode, Li metal cannot be employed for practical applications [10]. In comparison with lithium counterpart, Mg metal anode has shown a lower tendency to form dendrites entailing an improvement of the energy density at the materials' level [2, 6, 11, 12].

PANI is present in various forms depending on its oxidation levels [13]. The fully reduced and oxidized forms of PANI are known as leucoemaraldine and pernigraniline base, respectively. The half oxidized PANI is the emeradine base [14]. Among these, emeraldine is the most stable and conductive form exhibiting a conductivity in the range of 10^{-10} S cm^{-1} but its salt form has a conductivity of 30 S cm^{-1} [15]. The preparation of PANI-based nanocomposites with TiO_2, Fe_3O_4, Fe_2O_3 and ZrO_2 nanoparticles is supposed to be a potential way to attain materials with enhanced properties (electrochemical, optical, conductivity, catalytic, etc.) due to the synergistic effect of both PANI and inorganic particles [16–20].

The $MgCoO_2$ material has been scarcely used for battery storage applications, so far. It found applicability in aqueous Li- and Na-ion supercapacitor, alkaline HER electrocatalyst and generation of bioelectricity [21, 22]. Its divalent charge character allows achieving a theoretical capacity of 465 mA h g^{-}

[1]. Irrespective of the inherent problems of cobalt as one of the battery components due to the price and toxicity, cobalt has been extensively employed demonstrating several advantages attributed to its insertion and/or redox chemistry in batteries providing fundamental knowledge [23]. In this work we employed the cubic $MgCoO_2$ and polyaniline (PANI) as a conductive coating to prepare PANI@$MgCoO_2$ nanocomposites with suitable morphology and enhanced electrode/electrolyte interphase properties for applications in Mg battery. Na^+ is chosen to circumvent the inherent problems of Mg^{2+} diffusion through the host structure and showed potential advantage in low cost by avoiding the use of Li in the cathode and/or electrolyte [12, 24]. This work could represent an example for developing magnesium-based materials for energy storage and conversion applications [25].

2. Experimental Section

Preparation of polyaniline and chemical reagents: Aniline monomer is purified by double vacuum distillation. Ammonium persulfate ($(NH_4)_2S_2O_8$, APS) is used as an oxidant. Toluene and hydrochloric acid are used as received without further purification. MgO, nitric acid, Co $(NO_3)_2{\cdot}6H_2O$, and triethanolamine, are used to synthesize $MgCoO_2$.

Sol-gel preparation of $MgCoO_2$ particles: the $MgCoO_2$ particles are synthesized by sol-gel process using the triethanolamine as a chelating agent. 0.2015 g of MgO are dissolved in 10 ml nitric acid. In another beaker, we dissolve 1.4552 g of $Co(NO_3)_2{\cdot}6H_2O$ into 40 ml of deionized water. After forming a clear solution, the MgO and $Co(NO_3)_2{\cdot}6H_2O$ are mixed to prepare 50 mL of the reaction mixture. In the resultant solution, triethanolamine is added dropwise, which acts as a chelating agent. The reaction mixture is magnetically stirred at 150 ºC overnight until the solution formed a gel. The gel is dried for 12 h and ground to get a fine powder. Then, the powder calcinated for 5 h at 900 °C.

Synthesis of PANI@$MgCoO_2$ nanocomposite materials: the PANI@$MgCoO_2$ nanocomposites are prepared in a $MgCoO_2$ nanoparticle stabilized Pickering emulsion. To prepare the Pickering emulsion, the $MgCoO_2$ is firstly dispersed in water using an ultrasonic disperser Bandelin Sonorex TK52. The oil phase solutions consisted of aniline dissolved in toluene. The oil and aqueous phases are mixed with the ultrasound disperser during 2 min, and the emulsions are prepared at different ratio of aniline (5, 4, 3, and 1 wt.%). The pH value of the Pickering emulsion is adjusted to 4.5 using 2M HCl solution. Polymerization is carried under stirring in a cold bath (0 to 5 °C) by slow addition of APS solution. Then, the precipitate is washed with water and ethanol to remove salts, organic impurities, and PANI oligomers. The recovered powder is treated at 60°C under vacuum. PANI is prepared by in situ polymerization of aniline using ammonium persulfate ($(NH_4)_2S_2O_8$) as an oxidant in acidic medium in the presence of HCl solution.

Chemical and electrochemical characterization: X-ray diffraction patterns (XRD) of powder samples are performed with a Rigaku Ultima IV and Bruker D8 Discover A25 powder diffractometer with Cu Ka radiation (λ = 1.5406 Å) from 10 to 80° at a scan speed of $2°min^{-1}$. Rietveld refinements of XRD data are carried out by GSAS software [26,27]. Raman measurements are performed using a Renishaw Raman

instrument equipped with an InVia Raman microscope using green laser light with 532 nm radiation. The scanning electron microscopy (SEM) images are obtained using a Zeiss Sigma (Germany) microscope. Cation compositions of the samples are determined by inductively coupled plasma-atomic emission spectrometry (ICP, Thermo Electron).

Galvanostatic charge–discharge cycling measurements are conducted in 2025-type coin cells with Mg metal anode and 1 M $NaClO_4$ in propylene carbonate and fluoroethylene carbonate (PC:FEC, 95:5 vol.) electrolyte that are assembled inside an argon-filled glovebox. Mg metal is washed with a diluted solution of acid, rinsed with water and dried under argon flow prior to be used. A Neware battery testing station with a temperature control chamber (30°C) is used. The working positive electrode is formulated by mixing of 70 wt% of nanocomposite or pristine oxide, 20 wt% of carbon black and 10 wt% of the polyvinylidene fluoride (PVDF) as binder. The capacity value is calculated considering the mass of the cathode. The electrochemical impedance spectra (EIS) are measured in a four-channel multifunctional electrochemical workstation (Versa STAT MC. America) by applying 5 mV amplitude over a frequency range of 100 kHz to 2 mHz. The impedance circuit consists of the resistances of the electrolyte (Re), the surface layer (Rsl) and the charge-tansfer (Rct). The Warburg element, constant phase element and capacitor are represented with W, CPF and C, respectively.

3. Results And Discussion

The Rietveld refinements of XRD patterns of pristine $MgCoO_2$ and 1–5%PANI@$MgCoO_2$ nanocomposites are shown in Fig. 1. The diffraction pattern of $MgCoO_2$ displayed sharp Bragg reflexions (111), (200), (220) (311) and (222) that are indexed to a cubic structure with a well-established *Fm3m* space group, in agreement with previous reports in the literature [21, 22]. From the XRD peak positions, we have calculated the lattice parameters as a = b = c = 4.2369 (1) Å, and α = β = γ = 90º. Fig. S1 shows the XRD patterns of all the nanocomposites in the 10–80º range, and PANI shows four broad reflections between 10–30º owing to the periodicity parallel and perpendicular to the polymer chains [28, 29]. After PANI coating, the 1–5%PANI@$MgCoO_2$ nanocomposites materials are indexed also using the cubic *Fm3m* space group. The refined lattices and coherent domain sizes are given Fig. 1. Compared to the pristine $MgCoO_2$, the parameters ‘a’ and ‘V’ of PANI@$MgCoO_2$ nanocomposites remained invariant without affecting the crystal structure.

SEM micrographs revealed that synthesized $MgCoO_2$ exhibits flat and cube-shaped irregular particles with an average diameter of 0.5–0.6 µm. The micrographs of 1–5%PANI@$MgCoO_2$ nanocomposites revealed the presence of small grains of 80–100 nm and rough texture demonstrating that the small PANI grains are embedded on the $MgCoO_2$ particle surface. It is evidenced the structural flexibility of PANI (from 1%, 3%, 4–5%) on coating these sub-micrometric $MgCoO_2$ particles. In addition, the PANI is detected by a progressive appearance of nitrogen atom as recorded from the mapping together with the homogeneously dispersed magnesium, cobalt, and oxygen (Fig. S2). The effect of coating with PANI can facilitate the ion transportation and enhance electron transfer and influence the electrochemical

performance [30]. During the synthesis, emeraldine base is transformed into emeraldine salt as shown in Fig. 2F with benzenoid and quinoid rings in the PANI chains. The dependence of physicochemical properties on the synthesis conditions are among the most important PANI properties.

Raman spectra of PANI, $MgCoO_2$ and PANI@$MgCoO_2$ nanocomposites are plotted in Fig. 3. For $MgCoO_2$, three Raman-active bands can be observed (A_{1g}, E_g, and one F_{2g}). The A_{1g} peak at 687 cm^{-1} represents the metal-O bond vibrations of the octahedral sublattice [31], noting that it is the Raman vibration peak with the highest intensity out of the three, indicating that the cobalt cations mostly occupy the octahedral site. The F_{2g} peak at roughly 520 cm^{-1}, shows the stretching vibration of the Co-O bond. The E_g mode at ~ 478 cm^{-1} is caused by stretching of Mg-O and Co-O bonds in the tetrahedral sublattice [32]. For the PANI (emeraldine salt), Raman band at 1604 cm^{-1} is related to the C–C stretching vibration of benzene ring. The intense band observed at 1170 cm^{-1} is assigned to C–H vibrations of aromatic rings [33]. The bands at 874, 812 and 414 cm^{-1} correspond to out-of-plane deformations of the rings protonated emeraldine form of PANI [34]. The Raman spectra of PANI@$MgCoO_2$ (1, 3, 4 and 5 wt. %) nanocomposites are quite similar with a higher contribution of carbon bands as PANI content increases. No additional peaks are observed in the spectra, indicating that no chemical reactions between PANI and $MgCoO_2$ occurred.

To verify the advantages of the PANI@$MgCoO_2$ nanocomposite as cathode material for RMBs, the electrochemical discharge/charge behavior and cyclability are investigated (Figure 4A-D) using twofold ion approach (Na^+/Mg^{2+}). Previously, the limitations to perform the Mg-cell with pure $Mg(TFSI)_2$+DME electrolyte are confirmed. The galvanostatic curves of pristine $MgCoO_2$, 3%PANI@$MgCoO_2$ and 5%PANI@$MgCoO_2$ during the initial ten cycles at 5 mA g^{-1} are selected. During the first discharge a common characteristic in the reactions is observed: i) two plateau at 2.1 and 1V (labeled as 1 and 2 respectively), and ii) a constant decay of the potential in 1–0.05 V (labeled as 3). On the subsequent charge the curves show an extended plateau (between 4-4.5V) and the cell exhibit high polarization, and all the samples recovered around 99% of the capacity. Regarding the capacity, on increasing the PANI content (1, 3, 4 and 5%) the first discharge capacity increaseded from 147.9 (for pristine $MgCoO_2$) to 154.2, 172, 190.1, and 207.8 mA h g^{-1}, respectively (Fig. 4D). These capacities are lower than the theoretical capacity of $MgCoO_2$. On cycling, the first reversible capacities are respectively 99.3, 103.4, 125, 130.2 and 153 mA h g^{-1} which are retained 63% (62.8 mA h g^{-1}), 77% (80.3 mA h g^{-1}), 77% (95.7 mA h g^{-1}), 51% (66.2 mA h g^{-1}) and 48% (73.2 mA h g^{-1}) over 40 cycles. Most probably, polyaniline could not tolerate high-voltage oxidation, and the capacity decays constantly while cycling. However, the best synergistic effect is found for 1%PANI@$MgCoO_2$ and 3%PANI@$MgCoO_2$ with 65 and 68% of capacity retention up to 60 cycles, respectively.

According to the ex-situ XRD patterns the cubic phase persist after the complete discharge and discharge/charge and consequently a conversion reaction can be discarded in this system (Fig. 5). The peaks at 36.68, 42.64, 61.91, and 74.23° are assigned to the (111), (200), (220) (311) lattice planes of

cubic $MgCoO_2$ (Fig. S3) The aluminium current collector peaks are detected at 38.43, 44.68, 65.05 and 78.17º. The cell parameters at the end of the first discharge and discharge/charge do not show obvious variation for pristine $MgCoO_2$, 3%PANI@$MgCoO_2$ (65%) and 5%PANI@$MgCoO_2$ nanocomposites (4.2377(2)/4.2373(1) Å, 4.2379(2)/ 4.2378(1) Å and 4.2374(3)/ 4.2375(1) Å) as compared to the uncycled electrodes, and the cell volume slightly varied (see table S1). Then, an insertion reaction occurs and could be exemplified for these two samples as follows:

$MgCoO_2 + 0.64\ e^- + x\ Na^+ + y\ Mg^{2+} \leftrightarrow Mg_{1+y}Na_xCoO_2$ Eq. [1]

3%PANI@$MgCoO_2 + 0.9\ e^- + x\ Na^+ + y\ Mg^{2+} \leftrightarrow$ 3%PANI@$Mg_{1+y}Na_xCoO_2$ Eq. [2]

To quantify the amount of reacted sodium and/or magnesium, the galvanostatic profile in the Na-cell is performed for reference, which is reflecting that the total discharge capacity is 95 mA h g^{-1} with an extension of the reaction at points 1, 2 and 3 of 45, 15 and 35 mA h g^{-1}, respectively (Fig. S4). That behavior differs in terms of capacity to those observed in Mg-cell. Therefore, at points 1, 2 and 3 (Fig. 4A-C), a sequential insertion of Na/Mg into the cubic structure is occuring through a single-phase mechanism. This outcome differs to previous results where the insertion reaction into 3d transition metal oxides implies a two phase reaction mechanism [35–38]. Also, the insertion of lithium into $LiCoO_2$ cathode (2–4.5 V) is accompained by several phase transitions (hexagonal, monoclinic) leading to internal stress generation [23]. The ICP results confirmed the Mg:Na:Co atomic ratio for pristine electrode is 0.998:0:1.005 and after discharge in Na- and Mg-cells is 0.995:0.397:1.006 and 1.112:0.405:1.015, respectively (Table 1). Then, the extra capacity is due to the participation of Mg^{2+} ion in the insertion reaction. For 3%PANI@$MgCoO_2$ the atomic ratio in the discharged Mg-cell is 1.154:0.415:0.099 and after the subsequent charge allowed extraction of Mg and Na, as also found in pristine electrode. These results suggest reversible insertion/de-insertion into/from cubic $MgCoO_2$, whose findings show a different mechanism of reaction as compared to the reported conversion reactions (recorded between 0.01–3 V) in $LiCoO_2$ and Co_3O_4 when cycled versus metallic Li and Na anodes[39–41]. Aditionally, it should be noted the differences of the cubic $MgCoO_2$ compared to the oxyspinel MgM_2O_4 (M = Mn, Co, Ni) reacting with Mg through a biphasic reaction in which the main problem of Mn^{3+}/Mn^{+4} redox couple is the transformation from cubic to tetragonal spinel diminishing the ionic conductivity due to the smaller ion diffusion chanels in tetrgonal phase [42–44]. Therefore, cubic $MgCoO_2$ exhibit analogous structural characteristics as those in the cubic Mg_2MnO_4 [6] and $Mg_xNi_yCo_zO_2$ where the Co and Mg compositions were considered to facilitate the insertion/deinsertion of Mg^{2+} [45] .

Table 1
ICP results showing the Mg:Na:Co atomic ratio of pristine $MgCoO_2$ and 3%PANI@$MgCoO_2$ after first discharge and discharge/charge (at 5 mA g^{-1}) in Mg-cells with $NaClO_4$-PC:FEC electrolyte. For the sake of comparison, pristine $MgCoO_2$ is measured at the end of the discharge and discharge/charge in the sodium cell.

Sample		Capacity (mA h g^{-1})	Mg : Na : Co (ICP)	Remarks
$MgCoO_2$	Pristine	–	0.998 : 0 : 1.005	Pristine
$MgCoO_2$	Disch.	95	0.995 : 0.397 : 1.006	Na-cell
	Disch/Ch.	95 / 46	1.008 : 0.175 : 0.097	Na-cell
$MgCoO_2$	Disch.	147.9	1.112 : 0.405 : 1.015	Mg-cell
	Disch/Ch.	147.9 / 149	1.013 : 0.021 : 1.007	Mg-cell
3%PANI@$MgCoO_2$	Disch.	172	1.154 : 0.415 : 0.099	Mg-cell
	Disch/Ch.	172 / 171.9	1.017 : 0.011 : 1.012	Mg-cell

Some properties of the electrode/electrolyte interphase and kinetic response are studied from the impedance spectra for pristine, 3% and 5%PANI@$MgCoO_2$ after 30 cycles. Nyquist plots exhibit two semicircles revealing capacitive phenomena occurring at the surface layer (SL) and charge-transfer (CT) reactions at high and medium frequencies, respectively. The resistances decreased at the end of the discharge at 0.01 V for both coated samples ($R_{SL}^{3\%}$= 0.46 Ω·g $R_{CT}^{3\%}$= 0.92 Ω·g; $R_{SL}^{5\%}$= 0.59 Ω·g, $R_{CT}^{5\%}$= 1.25 Ω·g) as compared to the pristine sample (R_{SL}= 0.61 Ω·g, R_{CT}= 1.65 Ω·g). Additionally, the diffusion coefficients (D^+) are calculated at the quasi-equilibrium state using the following equation [46]:

$$D = \frac{1}{2}\left(\frac{RT}{SF^2\sigma_w C}\right)^2 \quad \text{Eq. [3]}$$

where R is the gas constant ($J{\cdot}K^{-1}{\cdot}mol^{-1}$), T is the absolute temperature, S is the area of the electrode surface, F is Faraday's constant, C is the molar concentration of Mg^{2+}/Na^+ ions and σ_w is the Warburg coefficient. The latter one is determined from the slope of Z' vs. the reciprocal root square of the lower angular frequencies ($\omega^{-1/2}$) in agreement with the following equation:

$$Z' = R_{SL} + R_{CT} + (\sigma_W \cdot \omega^{-1/2}) \quad \text{Eq. [4]}$$

Benefiting from synergistic effect of both PANI and $MgCoO_2$, the diffusion coefficient adopted these values: $6.92{\cdot}10^{-14}$ (3%PANI@$MgCoO_2$) > $4.18{\cdot}10^{-14}$ (5% PANI@$MgCoO_2$) > $3.05{\cdot}10^{-14}$ (pristine $MgCoO_2$) $cm^2\ s^{-1}$. These results are associated with an improvement of the kinetics of the charge transfer reaction on PANI coated samples.

Conclusions

Its firstly reported the synthesis and electrochemical properties of cubic $MgCoO_2$ and 15%PANI@$MgCoO_2$ nanocomposites for RMBs. PANI is uniformely coating the oxide particles and enhanced the cyclability and ion diffusion. The best sample exhibited 125 mA h g^{-1} reversible capacity at an average potential of ~ 1 V (vs. Mg^{2+}/Mg) which is retained 68% over 60 cycles. Most importantly, $MgCoO_2$ and its nanocomposites present a rigid framework for (de)-inserting Na/Mg ions with a single-phase reaction. The twofold ion approach can be accepted as a simple methodology to find other insertion oxides with applicability in RMBs.

Declarations

Conflict of interest. The authors declare no competing interests.

Funding

This work was partially supported by the Tunisian Ministry of Higher Education and Scientific Research. The National Key Research and Development Program of China and the National Natural Science Foundation of China supported these research activities. Also, Xiamen University Foreign Young Talents Program is acknowledged (project nº G2022149004L).

Author Contributions Statement

Kahla Missaoui: Investigation, Formal analysis, Validation and Writing - Original Draft

Karima Ferchichi: Conceptualization and Data curation.

Noureddine Amdouni: Validation and Conceptualization.

Daniel Cosano: Formal analysis.

Rui Liu: Formal analysis.

Siyuan Pan: Investigation.

He Zhanning: Investigation.

Yong Yang: Resources.

Gregorio F. Ortiz: Investigation, Supervision, Writing - Review & Editing and Funding acquisition.

All authors reviewed the manuscript.

References

1. Mao M, Gao T, Hou S, Wang C (2018) A critical review of cathodes for rechargeable Mg batteries. Chem. Soc. Rev. 47:8804-8841. https://doi.org/10.1039/C8CS00319J.
2. Kuang C, Zeng W, Li Y (2019) A Review of Electrode for Rechargeable Magnesium Ion Batteries. J. Nanosci. Nanotechnol. 19:12-25. https://doi.org/10.1166/jnn.2019.16435.
3. Rong Z, Malik R, Canepa P, Gautam G-S, Liu M, Jain A, Persson K, Ceder G (2015) Materials Design Rules for Multivalent Ion Mobility in Intercalation Structures. Chem. Mater. 27(17):6016–6021. https://doi.org/10.1021/acs.chemmater.5b02342.
4. Aurbach D, Lu Z, Schechter A, Gofer Y, Gizbar H, Turgeman R, Cohen Y, Moshkovich M, Levi E (2000) Prototype systems for rechargeable magnesium batteries. Nature 407:724–727. https://doi.org/10.1038/35037553.
5. Kitamura N, Konishi Y, Ma W, Ishida N, Mandai T, Ishibashi C, Idemoto Y, (2022) Positive-electrode properties and crystal structures of Mg-rich transition metal oxides for magnesium rechargeable batteries. Sci. Rep. 12:18097. https://doi.org/10.1038/s41598-022-23022-1.
6. Ruiz R, Pérez-Vicente C, Rubio S, Stoyanova R, Zuo W, Yang Y, Ortiz G-F (2022) A Cubic Mg_2MnO_4 Cathode for non-aqueous Magnesium Batteries. Energy Storage Mater. 48:12–19. https://doi.org/10.1016/j.ensm.2022.02.047.
7. Mohtadi R, Tutusaus O, Arthur T-S, Zhao-Karger Z, Fichtner, M (2021) The metamorphosis of rechargeable magnesium batteries. Joule 5:581-617. https://doi.org/10.1016/j.joule.2020.12.021.
8. Aurbach D, Suresh G-S, Levi E, Mitelman A, Mizrahi O, Chusid O, Brunelli, M (2007) Progress in Rechargeable Magnesium Battery Technology. Adv. Mater. 19:4260-4267. https://doi.org/10.1002/adma.200701495.
9. Manthiram A, Goodenough, J-B (2021) Layered lithium cobalt oxide cathodes. Nat. Energy 6:323. https://doi.org/10.1038/s41560-020-00764-8.
10. Goodenough J-B (2018) How we made the Li-ion rechargeable battery. Nat. Electron. 1:204. https://doi.org/10.1038/s41928-018-0048-6.
11. Davidson R, Verma A, Santos D, Hao F, Fincher C, Xiang S, Buskirk J-V, Xie K, Pharr M, Mukherjee P-P, Banerjee S (2019) Formation of Magnesium Dendrites during Electrodeposition. ACS Energy Lett. 4:375–376. https://doi.org/10.1021/acsenergylett.8b02470.
12. Li Y, An Q, Cheng Y, Liang Y, Ren Y, Sun C-J, Dong H, Tang Z, Li G, Yao Y (2017) A high-voltage rechargeable magnesium-sodium hybrid battery. Nano Energy 34:188–194. https://doi.org/10.1016/j.nanoen.2017.02.012.
13. Deshmukh K, Ahamed M-B, Deshmukh R-R, Khadheer Pasha S-K, Bhagat P-R, Chidambaram K (2017) Biopolymer Composites in Electronics, pp. 27-128. https://doi.org/10.1016/B978-0-12-809261-3.00003-6.
14. Zhou D-D, Cui X-T, Hines A, Greenberg R-J (2010) Conducting polymers in neutral stimulation applications, in: D.D. Zhao, E. Greenbaum (Eds.), Implantable Neural Prostheses, vol. 2, Springer, Berlin, pp. 217–252.

15. Blinova N-V, Stejskal J, Trchova M, Prokes (2008) Control of polyaniline conductivity and contact angles by partial protonation. J. Polym. Int. 57(1):66–69. https://doi.org/10.1002/pi.2312.
16. Xia H, Wang Q (2002) Ultrasonic Irradiation: A Novel Approach To Prepare Conductive Polyaniline/Nanocrystalline Titanium Oxide Composites. Chem. Mater. 14(5):2158–2165. https://doi.org/10.1021/cm0109591.
17. Aphesteguy J-C, Jacobo S-E (2007) Synthesis of a soluble polyaniline–ferrite composite: magnetic and electric properties. J. Mater. Sci. 42:7062–7068. https://doi.org/10.1007/s10853-006-1423-7.
18. Hsieh T-H, Ho K-S, Huang C-H, Wang Y-Z, Chen Z-L (2006) Electromagnetic properties of polyaniline/maghemite nanocomposites: I. The effect of re-doping time on the electromagnetic properties. Synth. Met. 156(21-24):1355–1361. https://doi.org/10.1016/j.synthmet.2006.10.005.
19. Wang S, Tan Z, Li Y, Sun L, Zhang T (2006) Synthesis, characterization and thermal analysis of polyaniline/ZrO_2 composites. Thermochim. Acta 441:191–194. https://doi.org/10.1016/j.tca.2005.05.020.
20. Prabhakar P-K, Raj S, Anuradha P-R, Sawant S-N (2011) Biocompatibility studies on polyaniline and polyaniline–silver nanoparticle coated polyurethane composite. Colloids Surf. B 86(1):146–153. https://doi.org/10.1016/j.colsurfb.2011.03.033.
21. Maitra S, Chakraborty P-K, Mitra R, Nath T-K (2020) Electrochemical aspects of sol-gel synthesized $MgCoO_2$ for aqueous supercapacitor and alkaline HER electrocatalyst applications. Curr. Appl Phys. 20(12):1404–1415. https://doi.org/10.1016/j.cap.2020.08.021.
22. Shetty B-H, Sundramoorthy A-K, Annamalai J, Murugan P, Atchudan R, Arya S, Alothman A-A, Ouladsmane M (2022) Fabrication of High-Performance MgCoO2/PEDOT:PSS@Nickel Foam Anode for Bioelectricity Generation by Microbial Fuel Cells. J. Nanomater. 2022:6358852. https://doi.org/10.1155/2022/6358852.
23. Lyu Y, Wu X, Wang K, Feng Z, Cheng T, Liu Y, Wang M, Chen R, Xu L, Zhou J, Lu Y, Guo B (2021) An Overview on the Advances of $LiCoO_2$ Cathodes for Lithium-Ion Batteries. Adv. Energy Mater. 11:2000982. https://doi.org/10.1002/aenm.202000982.
24. Rubio S, Liu R, Liu X, Lavela P, Tirado J-L, Li Q, Liang Z, Ortiz G-F, Yang Y (2019) Exploring the high-voltage Mg^{2+}/Na^{+} co-intercalation reaction of $Na_3VCr(PO_4)_3$ in Mg-ion batteries. J. Mater. Chem. A, 7:18081. https://doi.org/10.1039/C9TA05608D.
25. Li Q, Peng X-D, Pan F-S (2021) Magnesium-Based Materials for Energy Conversion and Storage. J. Magnes. Alloy. 9:2223-2224. https://doi.org/10.1016/j.jma.2021.11.003.
26. Toby B (2001) EXPGUI, Graphical User Interfaces for GSAS. J. Appl. Crystallogr. 34:210-213. https://doi.org/10.1107/S0021889801002242.
27. Larson A-C, Dreele R-B-V (2000) “GSAS: General structure analysis system report LAUR 86-748” Technical Report No. LAUR 86-748 (Los Alamos National Laboratory).
28. Moon Y-B, Cao Y, Smith P, Heeger A-J (1989) X-Ray Scattering from Crystalline Polyaniline. 196-199. Polym. Commun. 30:196-199.

29. Shi L, Wang X, Lu L, Yang X, Wu X (2009) Preparation of TiO_2/polyaniline nanocomposite from a lyotropic liquid crystalline solution. Synth. Met. 159(23-24):2525–2529. https://doi.org/10.1016/j.synthmet.2009.08.056.
30. Jing P, Lu H, Yang W, Cao Y, Xu B, Cai W, Deng Y (2020) Polyaniline-coated VS_4@rGO nanocomposite as high-performance cathode material for magnesium batteries based on Mg^{2+}/Li^+ dual ion electrolytes. Ionics 26(2):777–787. https://doi.org/10.1007/s11581-019-03239-3.
31. Wang Y, Sun J, Li S, Zhang Y, Xu C, Chen H (2020) Hydrothermal synthesis of flower-like $MgCo_2O_4$ porous microstructures as high-performance electrode material for asymmetric supercapacitors. J. Alloys Compd. 824:153939. https://doi.org/10.1016/j.jallcom.2020.153939.
32. Ya M, Wang J, Li G, Gao G, Zhao X, Cui J, Wu H, Li L (2023) Surface Engineering in $MgCo_2O_4$ Spinel Oxide for an Improved Oxygen Evolution Reaction. ACS Sustain. Chem. Eng. 11:744–750. https://doi.org/10.1021/acssuschemeng.2c06201.
33. Rohom B-A, Londhe U-P, Mahapatra S-K, Kulkarni S-K, Chaure N-B (2014) Electropolymerization of polyaniline thin films. High Perform. Polym. 26(6):641-646. https://doi.org/10.1177/0954008314538081.
34. Ferchichi K, Hbaieb S, Amdouni N, Pralong V, Chevalier Y (2013) Structural and electrochemical characterization of polyaniline/LiCoO2 nanocomposites prepared via a Pickering emulsion. J. Solid State Electrochem. 17:1432-8488. https://doi.org/10.1007/s10008-013-2014-6.
35. Thackeray M-M, David W-I-F, Bruce P-G, Goodenough J-B (1983) Lithium insertion into manganese spinels. Mater. Res. Bull. 18(4):461–472. https://doi.org/10.1016/0025-5408(83)90138-1.
36. Thackeray M-M, Baker S-D, Adendorff K-T, Goodenough J-B (1985) Lithium insertion into Co_3O_4: A preliminary investigation. Solid State Ion. 17(2):175-181. https://doi.org/10.1016/0167-2738(85)90069-4.
37. Thackeray M-M, de Picciotto L-A, de Kock A, Johnson P-J, Nicholas V-A, Adendorff K-T (1987) Spinel electrodes for lithium batteries - A review J. Power Sources 21(1):1–8. https://doi.org/10.1016/0378-7753(87)80071-X.
38. Larcher D, Masquelier C, Bonnin D, Chabre Y, Masson V, Leriche J-B, Tarascon J-M (2003) Effect of Particle Size on Lithium Intercalation into α Fe_2O_3. J. Electrochem. Soc. 150:A133. https://doi.org/10.1149/1.1528941.
39. Chadwick A-V, Savin S-L-P, Alcántara R, Lisbona D-F, Lavela P, Ortiz G-F, Tirado J-L (2006) X-ray Absorption Spectroscopic Study of $LiCoO_2$ as the Negative Electrode of Lithium-Ion Batteries. Chem. Phys. Chem. 7:1086–1091. https://doi.org/10.1002/cphc.200500619.
40. Chen Y, Chen X, Zhang Y (2021) A Comprehensive Review on Metal-Oxide Nanocomposites for High-Performance Lithium-Ion Battery Anodes. Energy Fuels 35(8):6420–6442. https://doi.org/10.1021/acs.energyfuels.1c00315.
41. Klein F, Jache B, Bhide A, Adelhelm P Phys. (2013) Conversion reactions for sodium-ion batteries. Chem. Chem. Phys., 15:15876-15887. https://doi.org/10.1039/C3CP52125G.

42. Ishibashi C, Mizutani Y, Ishida N, Kitamura N, Idemoto Y (2019) Crystal and Electronic Structures of $MgCo_{2-x}Mn_xO_4$ as Cathode Material for Magnesium Secondary Batteries Using First-Principles Calculations and Quantum Beam Measurements. Bull. Chem. Soc. Jpn. 92(12):1950-1959. https://doi.org/10.1246/bcsj.20190207.
43. Michail A, Silván B, Tapia-Ruiz N (2022) Progress in high-voltage $MgMn_2O_4$ oxyspinel as a cathode material in Mg batteries. Curr. Opi. Electrochem, 31:100817. https://doi.org/10.1016/j.coelec.2021.100817.
44. Truong Q-D, Kobayashi H, Nayuki K, Sasaki Y, Honma I (2020) Atomic-scale observation of phase transition of $MgMn_2O_4$ cubic spinel upon the charging in Mg-ion battery. Solid State Ion. 344:115-136. https://doi.org/10.1016/j.ssi.2019.115136.
45. Idemoto Y, Takahashi T, Ishida N, Nakayama M, Kitamura N (2019) Synthesis, Crystal Structure Analysis, and Electrochemical Properties of Rock-Salt Type $Mg_xNi_yCo_zO_2$ as a Cathode Material for Mg Rechargeable Batteries. Inorg. Chem. 58(9):5664–5670. https://doi.org/10.1021/acs.inorgchem.8b03638.
46. Shenouda A-Y, Liu H-K J. (2010) Preparation, Characterization, and Electrochemical Performance of Li_2CuSnO_4 and $Li_2CuSnSiO_6$ Electrodes for Lithium Batteries. J. Electrochem. Soc. 157:A1183-A1187. https://doi.org/10.1149/1.3479425.

Figures

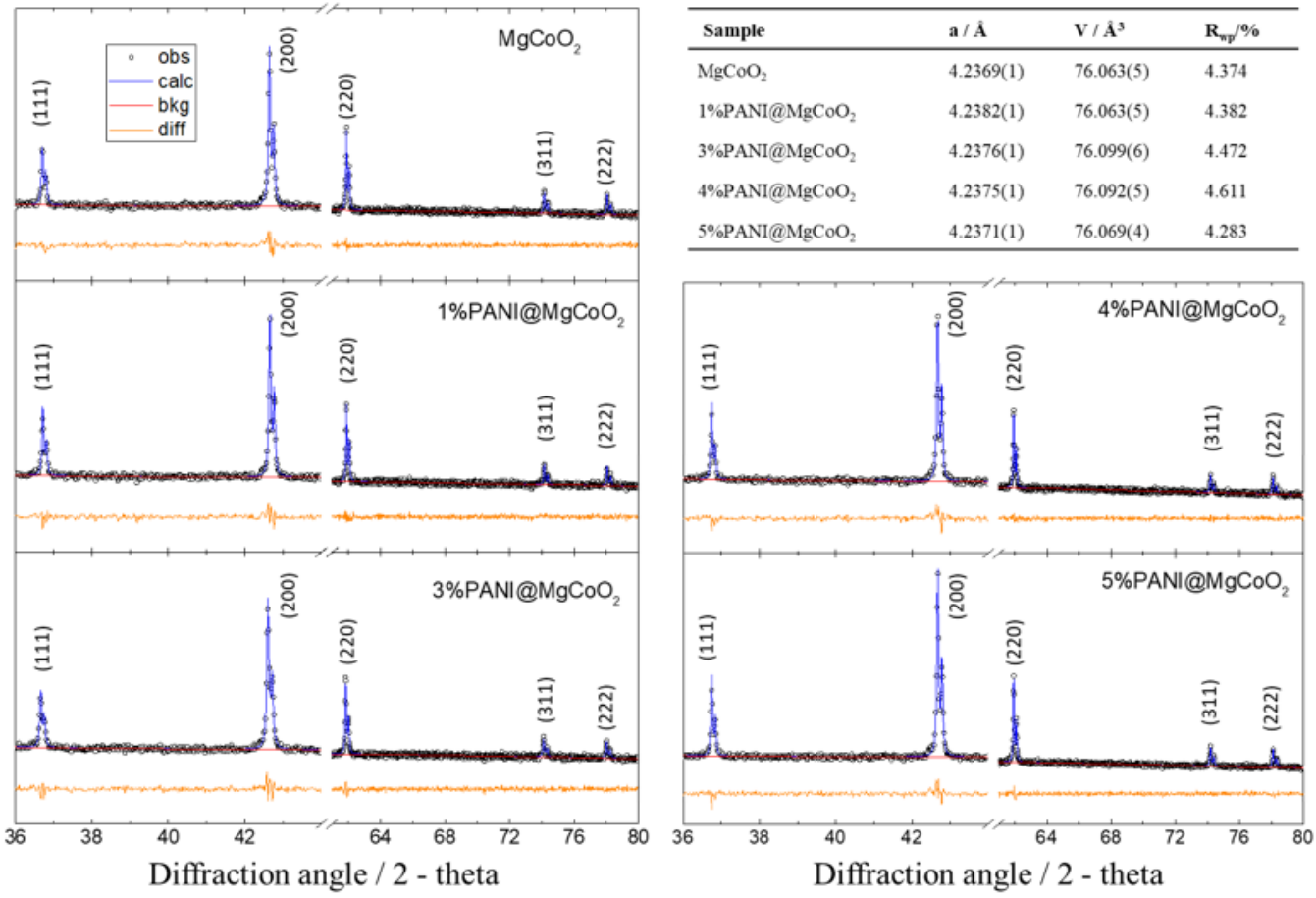

Sample	a / Å	V / Å^3	R_{wp}/%
$MgCoO_2$	4.2369(1)	76.063(5)	4.374
1%PANI@$MgCoO_2$	4.2382(1)	76.063(5)	4.382
3%PANI@$MgCoO_2$	4.2376(1)	76.099(6)	4.472
4%PANI@$MgCoO_2$	4.2375(1)	76.092(5)	4.611
5%PANI@$MgCoO_2$	4.2371(1)	76.069(4)	4.283

Figure 1

Rietveld refinement of the XRD patterns of pristine $MgCoO_2$ and 1, 3, 4 and 5%PANI@$MgCoO_2$ nanocomposites using the cubic *Fm-3m* symmetry. The table includes the unit cell parameters and R_{wt}.

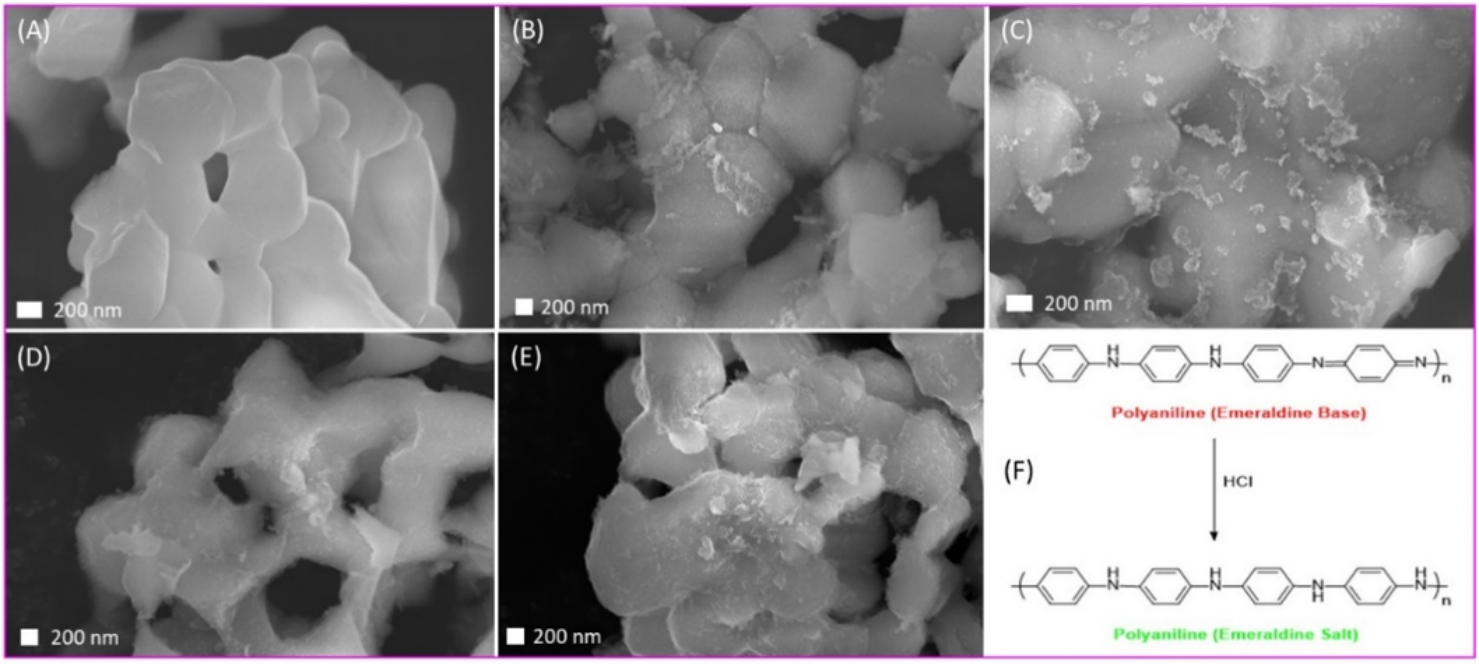

Figure 2

FE-SEM images of: (A) pristine $MgCoO_2$, (B) 1%PANI@$MgCoO_2$, (C) 3%PANI@$MgCoO_2$, (D) 4%PANI@$MgCoO_2$, and (E) 5%PANI@$MgCoO_2$ nanocomposites. (F) Structure of polyaniline showing the transformation from emeraldine base to emeraldine salt.

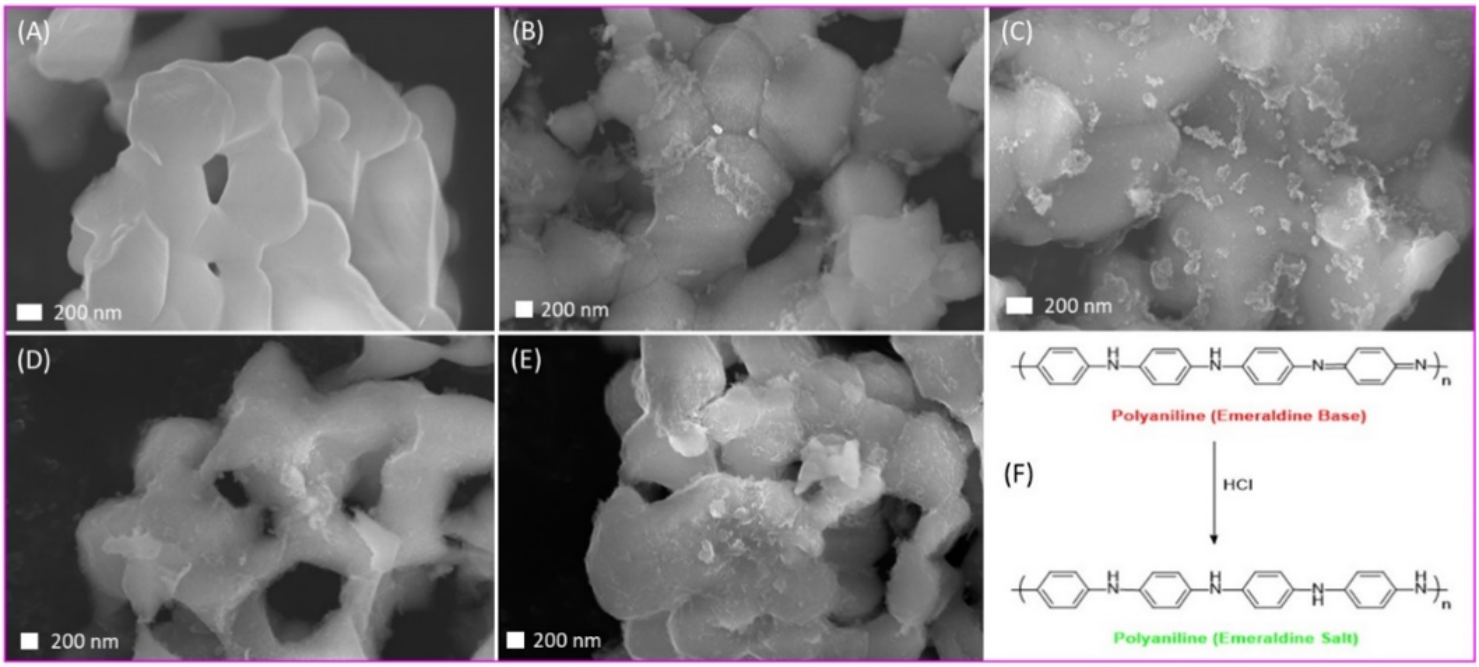

Figure 3

Raman spectra of PANI, pristine $MgCoO_2$ and 1-5%PANI@$MgCoO_2$ nanocomposites.

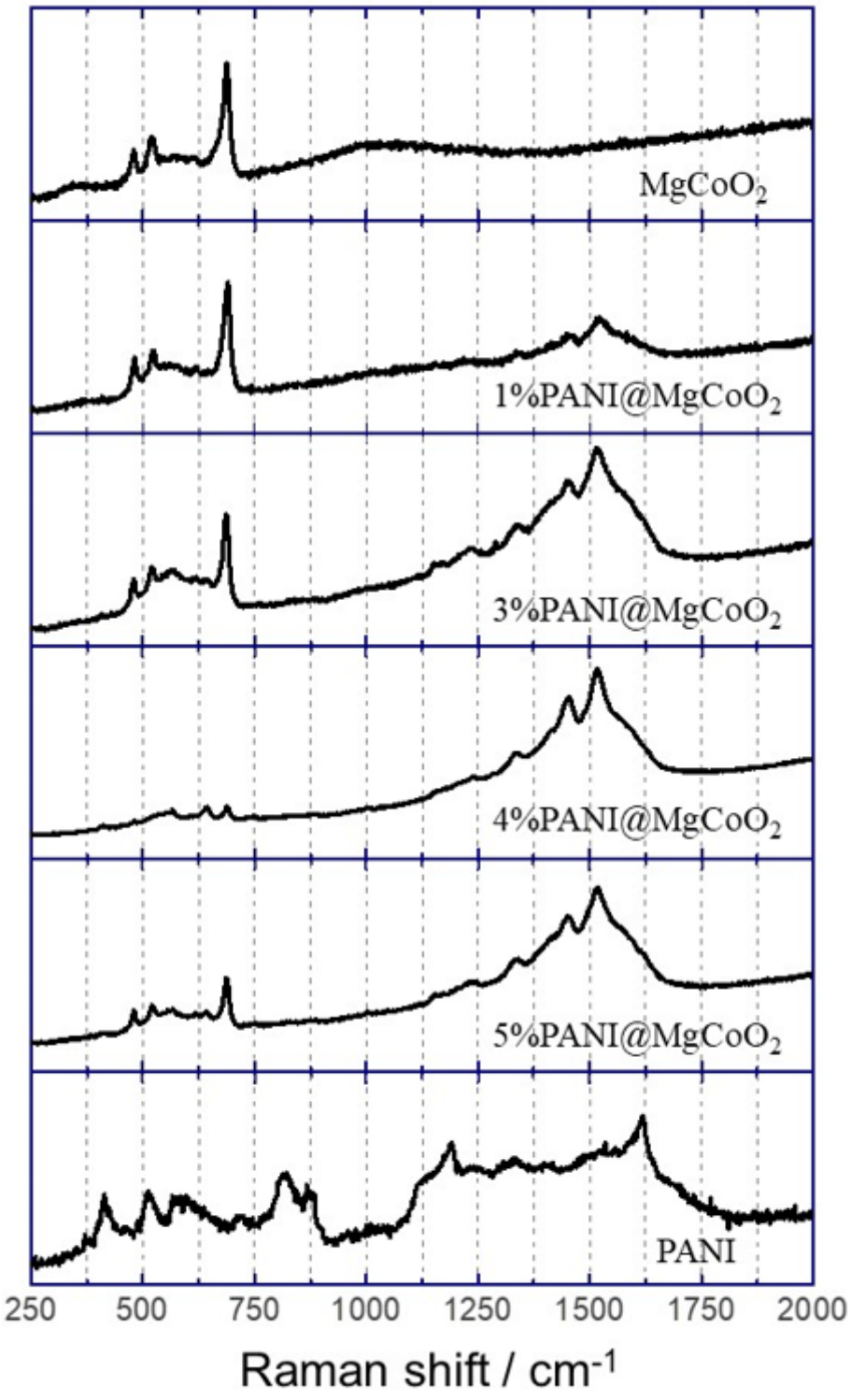

Figure 4

Galvanostatic profile of: (A) pristine $MgCoO_2$, (B) 3%PANI@$MgCoO_2$, and (C) 5%PANI@$MgCoO_2$ nanocomposites. (D) Capacity retention vs cycle number of all the samples.

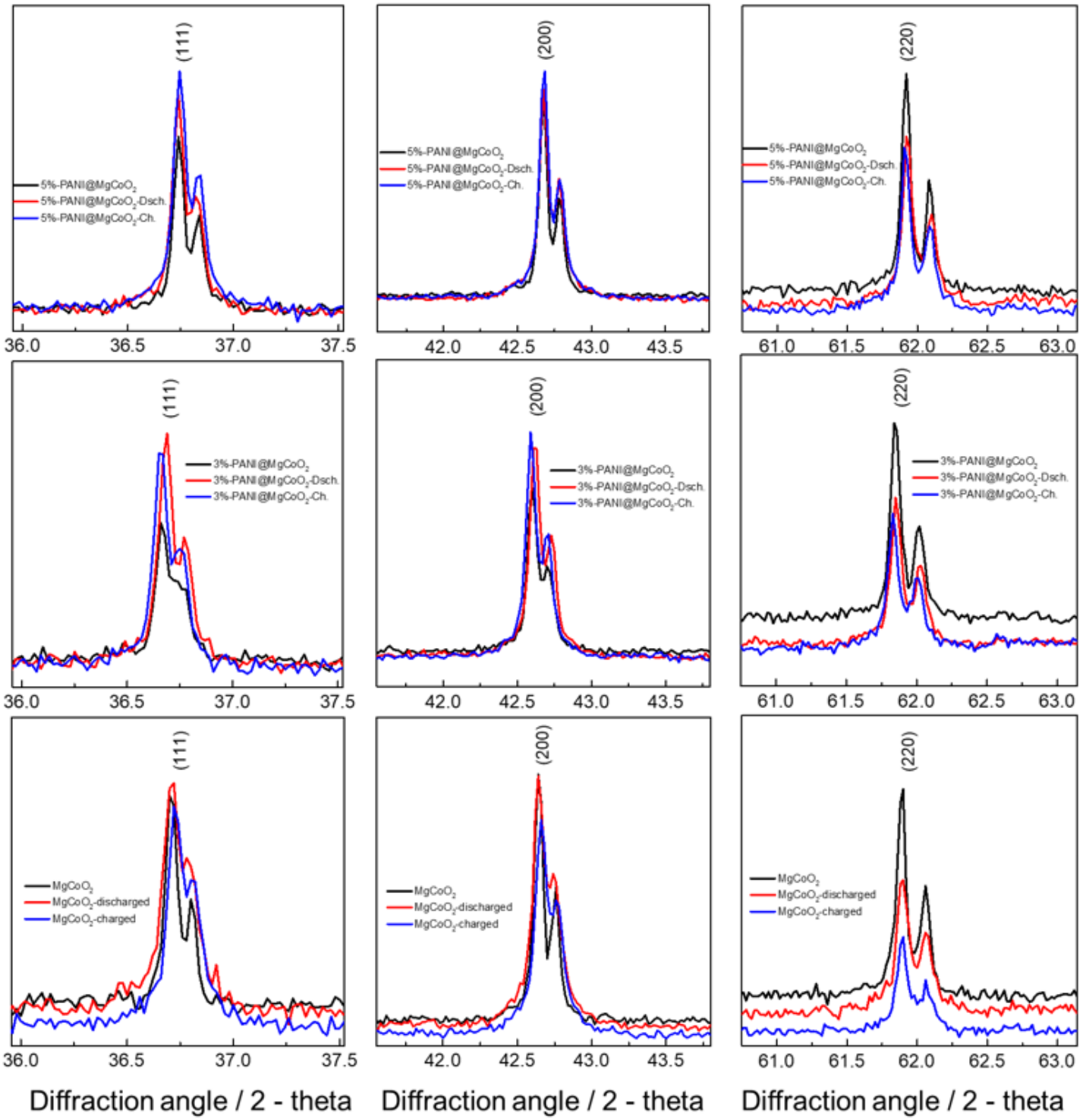

Figure 5

Ex-situ XRD patterns of pristine $MgCoO_2$, 3%PANI@$MgCoO_2$, and 5%PANI@$MgCoO_2$ nanocomposites after a complete discharge and discharge/charge.

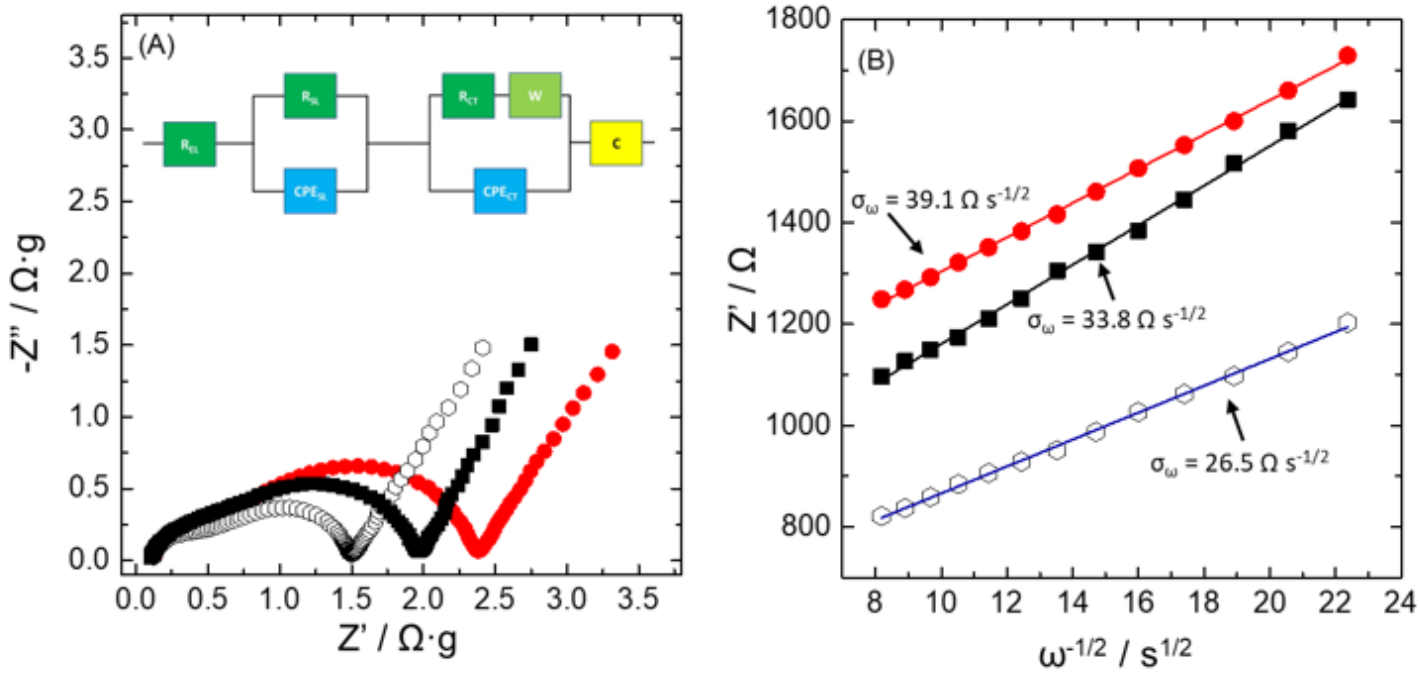

Figure 6

(A) Nyquist plots of pristine (red filled symbol), 3%PANI@$MgCoO_2$ (black open symbols) and 5%PANI@$MgCoO_2$ (squared filled symbols). The inset shows the equivalent circuit employed for the fitting. (B) Z' vs. the reciprocal frequency ($\omega^{1/2}$) for the samples described in part (A). The data are fitted for the calculation of Warburg coefficient (σ_ω).

Supplementary Files

This is a list of supplementary files associated with this preprint. Click to download.

- supportinginformationMgCoO220230322.docx